Computerized Medical Imaging and Graphics 46 (2015) 56–63

Contents lists available at ScienceDirect

Computerized Medical Imaging and Graphics

journal homepage: www.elsevier.com/locate/compmedimag

Sparse group composition for robust left ventricular epicardium segmentation

Bing Wang[a], Xiaomeng Gu[b], Chonghao Fan[b], Hongzhi Xie[c,*], Shuyang Zhang[c], Xuedong Tian[d], Lixu Gu[b,e,**]

[a] College of Mathematics and Information Science, Hebei University, Baoding, China
[b] Multi-disciplinary Research Center, Hebei University, Baoding, China
[c] Department of Cardiovascular, Peking Union Medical College Hospital, Beijing, China
[d] College of Computer Science, Hebei University, Baoding, China
[e] School of Biomedical Engineering, Shanghai Jiao Tong University, Shanghai, China

ARTICLE INFO

Article history:
Received 23 January 2015
Received in revised form 20 June 2015
Accepted 22 June 2015

Keywords:
LV epicardium segmentation
Sparse group composition
Multi-shape prior modeling
Gradient Chan-Vese (GCV) model

ABSTRACT

Left ventricular (LV) epicardium segmentation in cardiac magnetic resonance images (MRIs) is still a challenging task, where the a-priori knowledge like those that incorporate the heart shape model is usually used to derive reasonable segmentation results. In this paper, we propose a sparse group composition (SGC) approach to model multiple shapes simultaneously, which extends conventional sparsity-based single shape prior modeling to incorporate a-priori spatial constraint information among multiple shapes on-the-fly. Multiple interrelated shapes (shapes of epi- and endo-cardium of myocardium in the case of LV epicardium segmentation) are regarded as a group, and sparse linear composition of training groups is computed to approximate the input group. A framework of iterative procedure of refinement based on SGC and segmentation based on deformation model is utilized for LV epicardium segmentation, in which an improved shape-constraint gradient Chan-Vese model (GCV) acted as deformation model. Compared with the standard sparsity-based single shape prior modeling, the refinement procedure has strong robust for relative gross and not much sparse errors in the input shape and the initial epicardium location can be estimated without complicated landmark detection due to modeling spatial constraint information among multiple shapes effectively. Proposed method was validated on 45 cardiac cine-MR clinical datasets and the results were compared with expert contours. The average perpendicular distance (APD) error of contours is 1.50 ± 0.29 mm, and the dice metric (DM) is 0.96 ± 0.01. Compared to the state-of-the-art methods, our proposed approach appealed competitive segmentation performance and improved robustness.

1. Introduction

Cardiovascular diseases (CVDs) are the number one cause of death globally [1]. An estimated 17.3 million people died from CVDs in 2008, representing 30% of all global deaths [1]. By 2030, the number of people who die from CVDs will increase to reach 23.3 million [1,2]. Non-invasive assessment of left ventricular function based on cardiac MRI is of great value for the diagnosis and treatment monitoring of these pathologies. For example, LV contractile function quantified through ejection fraction, myocardium mass and ventricle volume, are often used as a crucial indicator in the assessment of deficient blood supply to the cardiac tissue [3,4].Calculations of such measurements is dependent on accurate delineation of LV myocardial boundaries. However, reliable and accurate automatic delineation of cardiac inner wall and outer wall remains a difficult problem, due to intensity inhomogeneities of tissues outside myocardium, the poor contrast between these tissues and myocardium, papillary muscles connected to the inner myocardium wall, artifacts arising from flow and noise [3]. Some unreliable appearance cues in cardiac MRI images are demonstrated in Fig. 1.

Significant numbers of methods have been proposed for (semi-)automated LV segmentation, including approaches using no, weak, strong prior knowledge [3]. Methods that work with weak or

---

* Corresponding author at: Peking Union Medical College Hospital, Department of Cardiovascula, Beijing 100005, China. Tel.: +86 10 69156114.
** Corresponding author at: Shanghai Jiao Tong University, School of Biomedical Engineering, Med-X Research Institute, 1954 Huashan Road, Shanghai 200240, China. Tel.: +86 21 34204137.

E-mail addresses: xiehongzhi@medmail.com.cn (H. Xie), gulixu@sjtu.edu.cn (L. Gu).

http://dx.doi.org/10.1016/j.compmedimag.2015.06.003
0895-6111/© 2015 Elsevier Ltd. All rights reserved.

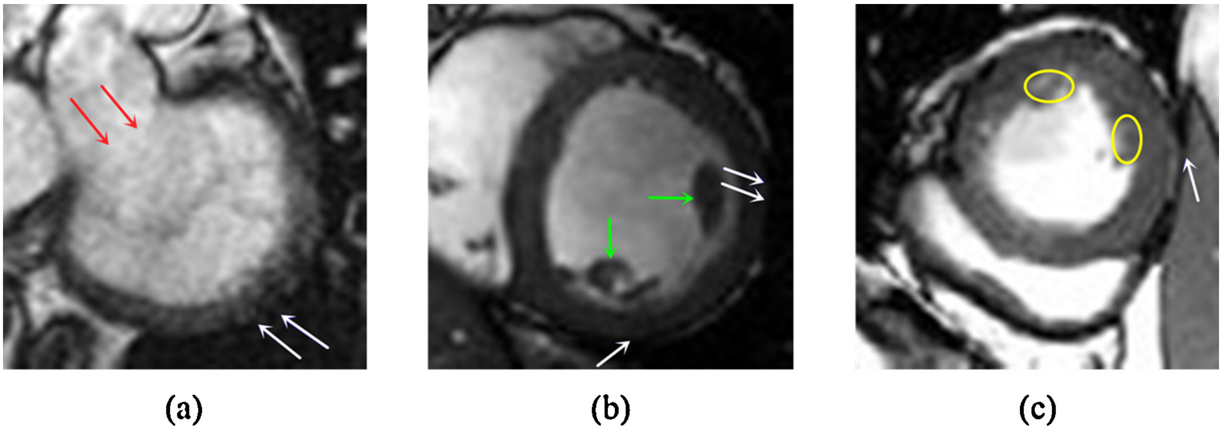

Fig. 1. Demonstration of several unreliable appearance cues in cardiac MRI images. (a) Missing border is pointed out by red arrows. Fuzzy borders are pointed out by white arrows. (b) Papillary muscles within the LV cavity are indicated by green arrows. (c) Muscles connected to the inner myocardium wall are surrounded by yellow ellipses. (For interpretation of the references to color in this figure legend, the reader is referred to the web version of this article.)

no prior knowledge, including methods based on thresholding [5], dynamic programming [6–9], clustering [10–12], and a combination of these [13–15], have been considered as general LV segmentation methods. Besides, graph-based methods, such as graph cut [16–18] and random walk [19], have been introduced that can achieve desired results with limited user-interaction. And, deformable model [20,21], such as active contour (or snake) model [22,23], level set [24], and their variants, have been prevalently applied in LV segmentation. However, almost all of these methods require manual intervention more or less.

In recent years, it has become widely recognized that integrate strong prior into aforementioned methods can be effective for medical image segmentation. Approaches that utilize strong prior knowledge have demonstrated great success in cardiac MRI and can be able to increase the final robustness and accuracy in the process of tackling LV segmentation tasks. Shape prior plays a significant role in these methods combining strong prior. Leventon et al. [25] defined a probability distribution over the variances of training shapes, and utilized it to constrain the flow of the geodesic active contour. Rousson et al. [47] introduced shape constraints to level set representations. Cremers et al. [26] incorporated statistical shape knowledge in the evolution process of a Mumford-Shah based segmentation [27]. In this area, Mahapatra et al. [28] use a single image from each dataset to get prior shape information and integrated prior shape constraints into a graph cuts framework for segmenting LV. Wu et al. [29] considered endocardium as a rough circle and applied a dynamic circle to constraint the snake model for its segmentation; and utilized its result as a prior shape of epicardium to constraint the segmentation through a shape-similarity based energy between evolution contour and endocardium. In recent years, active shape model (ASM) [30] and active appearance model (AAM) [31] have been proposed by Cootes et al. in 1995 and 1998, respectively, which are statistical shape models (SSMs) [43] of the distribution of a set of landmark points over a population of training samples. ASM is built up using a prior knowledge about the shape, usually hand-annotated segmentation from a training set of data. AAM is an extension of the ASM, except adding texture of the shape to the model. Hence, AAM represents both the shape and texture variability seen in a training set. Mitchell et al. [32] first presented AAM for the segmentation in 2D cardiac MR images. The method was later extended to a full 3D AAM [33]. Now, both ASM and AAM probably are two of the most popular methods in the segmentation of LV in 2D, 3D and 4D (3D + time) datasets. In [34], a combination of ASM and AAM was used to segment the left and right ventricles on 4D MR images. Atlas-based segmentation technique has also been used for heart segmentation, which can easily be propagated throughout the cardiac cycle using the same principle. Lorenzo-Valdes et al. [35] proposed an automatic atlas-based segmentation algorithm for 4D cardiac MR images. Zhang et al. [36] constructed an effective 3D shape atlas for LV from cardiac MRI data.

Sparsity theory was introduced into shape prior modeling by Zhang [37,38], named as sparse shape composition model (SSC). In their model, a sparse composition of training shapes is computed adaptively to infer/refine an input shape, which alleviates three problems in a unified framework, i.e., modeling complex shape variations, handling non-Gaussian errors and preserve local detail information of the input shape. Model assumes the given shape information may contain gross errors, but such errors are often very sparse. However, in the case of LV epicardium segmentation in cardiac MRIs, image noise or input shape errors might be gross and relatively dense, which degrades segmentation performance of these methods due to only modeling single prior shape. Considering the situation that epi- and endo-cardium are closely related two walls in myocardium, the spatial constraint in between them is supposed to be beneficial for the epicardium modeling. In this paper, we present an extension of SSC for epi- and endocardium modeling, that is, sparse group composition model (SGC), where epi- and endo-cardium are regarded as a group and modeled together. A framework of iterative procedure of refinement based on SGC and segmentation based deformation model is utilized for LV epicardium segmentation of cardiac MRI, in which an improved shape-constraint gradient Chan-Vese model (GCV) acted as deformation model [39–41,47]. The gradient vector energy acts as an effective image force to enhance the weak boundaries and partly inhibit overflow at fuzzy boundaries.

The main advantage of segmentation framework based on SGC is twofold: (1) for the given endocardial contour, a reasonable initial epicardial contour can be estimated solely from the endocardial contour based on SGC without complicated manual landmark detection; (2) it is capable of achieving more stable refinement result compared with conventional sparity-based single shape prior model even if image noise or input shape errors might be gross and relatively dense. Both properties of this extension have proven to be valuable in the epicardium segmentation process and can be merged into other segmentation methods conveniently.

2. Method

2.1. Sparse group composition model

Aiming at modeling multiple shapes simultaneously, SSC is improved into a coupled form to incorporate the prior spatial relevant information among them. Shapes may refer to shapes of different objects (e.g., shapes of femur bone, femur cartilage, tibia bone and tibia cartilage of one patient) or shapes of a time-varying object (e.g., shapes of heart).

Following SSC, explicit parametric shape representation is employed in this method. Let m represents the number of shapes required to be modeled. Vertex number and column vector of the ith shape are notated by k_i and $s^i \in \mathbb{R}^{k_i \times d}$ respectively, where d stands for the dimension of shapes. Group vector g can be constructed by concatenating s^i for $i = 1, 2, \ldots, m$, as shown in the following equation:

$$g \triangleq \left[s^{1T} s^{2T}, \ldots, s^{mT}\right]^T \in R^{\sum_i k_i \cdot d} \tag{1}$$

Assuming that there are n samples with manual delineation in the training repository, a matrix $D \in R^{\left(\sum_i k_i \cdot d\right) \times n}$ which represents the training repository is required to be constructed by pre-aligning training samples. Pre-alignment is aiming at transforming training samples into a standard coordinate system. Generally, when the training repository is relative insufficient, scale variation is needed to be removed despite scale variation is a valid part of shape variation. Same as SSC, alignment is achieved based on generalized procreates analysis [40].

The basic idea of SSC can be intuitionally extended to groups: for an input group $y_g = \left[y_1^T y_2^T \ldots y_m^T\right]^T$, an optimal sparse linear combination of existing training groups can be found to approximately represent it. Based on SSC, this problem can be formulated as:

$$\underset{x,e,\beta}{\operatorname{argmin}} \left\| T\left(y_g, \beta\right) - Dx - e \right\|_2^2 + \varphi_1 \|x\|_1 + \varphi_2 \|e\|_1 \tag{2}$$

where $T\left(y_g, \beta\right)$ is a global transformation operator with parameter β. It aligns the input group y_g to the mean group of existing data D. $x \in R^n$ denotes the linear composition coefficients, and the optimal value of x_{opt} can be found utilizing the optimization method proposed in [37]. Sparse vector $e \in R^{\left(\sum_i k_i \cdot d\right)}$ is used to model error of input group. φ_1 and φ_2 control how sparse x and e are, respectively. Higher φ_1 or φ_2 indicates higher weight in the energy, and leads to a more sparse x or e.

In additional, a diagonal matrix P can be modeled to give each shape a weight in the objective function. The problem is reformulated as:

$$\underset{x,e,\beta}{\operatorname{argmin}} \left\| PT\left(y_g, \beta\right) - PDx - e \right\|_2^2 + \varphi_1 \|x\|_1 + \varphi_2 \|e\|_1 \tag{3}$$

where P is in the following form:

$$P = \operatorname{diag}\left(\underbrace{w_1 \ldots w_1}_{k_1 \times d} \underbrace{w_2 \ldots w_2}_{k_2 \times d} \ldots \underbrace{w_m \ldots w_m}_{k_m \times d} \right) \tag{4}$$

Generally, $w_i\,(i = 1, 2, \ldots, m)$ should all be nonzero in order to incorporate the mutual information among these shapes. When P is multiplied by a positive constant, the final optimal composition coefficients x_{opt} will remain unchanged. Thus, w_i is suggested to be no larger than 1 for the convenience of parameter setting. Furthermore, when $w_i \neq 0$ and $w_j = 0\,(\text{for all } j, j \neq i)$, Eq. (3) is as same as SSC of the ith shape.

In the case of left ventricle modelling, outline is composed of both epi- and endo-cardial contours, and represented by the group of them. In this study, we build the same length of vectors and one-to-one point relationship between epi- and endo-cardium contours, which enables the similar optimization algorithm of standard SSC to SGC. Thus epi- and endo-cardium contours are represented with 32 equiangular sampling vertices, respectively through determining a line originating from LV center and pointing toward the right ventricle passing through the interventricular septum (as shown in Fig. 2).

2.2. Initial epicardium estimation

During the estimation of initial epicardium, epicardium landmark detection is quite complex, and the landmark detection and shape inference framework proposed in [37] is not directly suitable to SGC since marking landmarks both on epi- and endo-cardium require more manual manipulations. However, due to the same length of vectors and one-to-one point relationship between epi- and endo-cardium contours in their a-prior spatial constraint, we can advance this inference concept of shape from SSC into the group level, and regard the endocardial vertices as 'landmarks' of the shape group consisting of LVepi- and endocardium. For an input endocardium y_{endo}, group vector is formed by filling with zeros in the first place. Then, optimal composition coefficients is calculate with $w_{endo} = 1, w_{epi} = 0$, where w_{endo} and w_{epi} are endo- and epi-cardium weights corresponding to different w_i in formula (4). Assume input endocardial contour is given, in fact, the endocardium segmentation is intensively studied due to MRI provides quite good contrast between myocardium and the blood flow [3], thus the error term e is not modeled. Using EM algorithm to solve formula (3), x and β are calculated. Let $x_{opt} = x$, then the epicardium estimation is constructed through corresponding

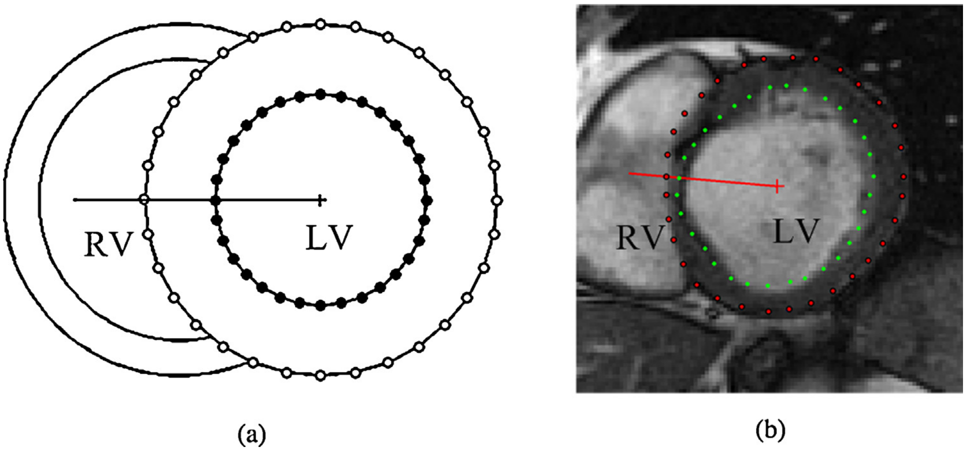

Fig. 2. Equiangular sampling. (a) Simple synthetic example in which epicardial vertices (hollow dots) and endocardial vertices (solid dots) are equiangular sampled from the slope angle; (b) Corresponding LV image where epi- and endo-cardium sample points are denoted in blue and green colours, respectively.

elements in $\mathrm{T}^{-1}\left(\mathrm{Dx}_{\mathrm{opt}}, \beta\right)$. By this means, landmark detection task is replaced by the endocardium delineation. And the rest of group, the epicardial contour in the case of LV epicardium segmentation can be inferred based on these 'landmarks' and SGC.

2.3. Epicardium refinement

In our study, the initial estimated contour serves as prior shape constraint term of the improved shape constraint GCV models described in following section to execute epicardium segmentation. Standard sparsity-based single prior shape modelling is capable of dealing with sparse gross errors, but the errors exited in the input shape might be too large and not sparse enough, which reduces availability of the model. To extend the ability of sparse shape composition to this situation, we form epi- and LV endocardium as a group and model spatial relationship between them. On the premise of accurate endocardium segmentation, the errors of input epicardial shape are sparse in the group representation. Thus, a-prior spatial constraint between them is also utilized in the refinement process to guide the input epicardial contour approach to the target position.

3. Segmentation based on Chan-Vese (CV) model

3.1. Improved shape constraint gradient Chan-Vese (GCV) model

Shape-constraint GCV [39] is an effective method for objects with weak and missing boundaries. It is derived from Chan-Vese model [41] by combining a gradient vector flow (GVF) energy term and a shape comparison function term. By minimizing the energy function, evolution contour is forced to approach the proper boundary. The Euler-Lagrange equation used for optimization is defined as:

$$\frac{\partial \phi}{\partial t} = \delta_{\varepsilon}(\phi)\left[\mu div\left(\frac{\nabla \phi}{\left|\nabla \phi\right|}\right) - \nu - \lambda_1 (u - c_1)^2 + \lambda_2 (u - c_2)^2\right] + \alpha \frac{\nabla \phi \cdot g}{\left|\nabla \phi\right| \cdot |g|} - 2\rho(\phi - \phi_B) = 0 \quad (5)$$

u represents the given image. ϕ is the level set representations of evolution contour C. ϕ_B is the level set representations of constraint contour. c_1 and c_2 indicates the average intensity inside and outside C, respectively. ν, μ, λ_1, λ_2, α and ρ are weighting parameters of each force term. The values of these parameters are empirically determined by a sufficient number of repeatable experiments. In our study, we select $\nu = 0$, $\mu = 0.15 \times 255^2$, $\lambda_1 = \lambda_2 = 1$, $\alpha = 0.5$ and $\rho = 0.05$ as proper parameters for final segmentation experiments.

However, due to the specificity of epicardium, this method is not directly applicable. Some alterations are required to be conducted. Segmentation of epicardium actually is to separate the myocardium from tissues outside. While blood pool surrounded by endocardium shows relatively strong contrast with the myocardium, evolution contour will get stuck into the endocardial wall if it's initialized inside the blood pool.

$\lambda_1(u - c_1)^2$ and $\lambda_2(u - c_2)^2$ in Eq. (5) can be regarded as indrawn and outward force filed based on pixel value, which measures the differences of pixels in image u from the target and outer region. Pixels with large difference with c_2 and small difference with c_1 are considered belong to the target object, and producing an outward force which drives the evolution contour to merge them, vice versa. However, intensity of tissues outside epicardium is quite inhomogeneous and complex, which provides poor contrast with the myocardium. Thus, average intensity outside C is not suitable to determine the membership of pixels. Considering the tissues surrounding epicardial wall which show good contrast with myocardium can be generally classified into two categories: brighter part and darker part. Reference intensities of these two parts are denoted as I_l and I_h. Then $\lambda_2 \cdot \min\left[(u - I_l)^2, (u - I_h)^2\right]$ is calculated as the new outward force, where pixels with brighter intensity or darker intensity are both considered belonging to the outer region. Average intensity inside evolution contour is also not the right parameter for measuring difference from myocardium, and should be replaced by the average intensity of myocardium, noted as I_{myo}. Note that I_l and I_h usually should be quite distinct to I_{myo}, in order to let myocardium pixels around the fuzzy border be classified into myocardium and overcome the tension. The evoking overflow is dealt with the shape constraint force. Furthermore, $\delta_{\varepsilon}(\phi)$ is multiplied onto the shape-constraint force field, which restrict the evolution in the neighborhood of current C.

Table 1
Epicardium segmentation framework.

Input: Target image and corresponding endocardium contour
Step 1: Initial epicardium estimation based on SGC
Step 2: Initial segmentation based on improved GCV model with estimated contour as constraint shape
Repeat
Step 3: Refinement based on SGC
Step 4: Deformation based on improved GCV with refinement result as constraint shape
Until reach max iteration time
Smoothness

The adapted Euler–Lagrange equation is defined as:

$$\frac{\partial \phi}{\partial t} = \delta_{\varepsilon}(\phi)\left\{\mu div\left(\frac{\nabla \phi}{\left|\nabla \phi\right|}\right) - \nu - \lambda_1\left(u - I_{\mathrm{myo}}\right)^2 + \lambda_2 \cdot \min\left[(u - I_l)^2, (u - I_h)^2\right]\right\} + \alpha \frac{\nabla \phi \cdot g}{\left|\nabla \phi\right| \cdot |g|} - 2\rho \cdot \delta_{\varepsilon}(\phi) \cdot (\phi - \phi_B) = 0 \quad (6)$$

As endocardium is the stronger feature in comparison with epicardium, GVF force guides evolution contour toward the opposite direction at the early evolution stage. At the later stage, complex surroundings around fuzzy borders produce misleading GVF force as well, which can be removed by setting α to 0.

3.2. Segmentation framework

Based on SGC and shape-constraint GCV, mutual information based left ventricular epicardium segmentation framework, as shown in Table 1, can be implemented. First, a reasonable epicardial contour is inferred based on the obtained endocardium and the implicit spatial relation between them. With such an estimation as constraint shape, deformation based on adopted shape-constraint GCV is conducted to acquire an initial segmentation. Then, an iterative deform-refine process is conducted to achieve accurate epicardium segmentation. Shape-constraint GCV is initialized at the endocardium to avoid evolution contour leaking at the weak edge in the second step. However, in the iterative process, it should be initialized at the refinement result to accelerate the segmentation speed.

4. Experiment

The datasets used for evaluation have been kindly made public by Radau et al. [42], which consists of 45 cardiac cine MR cases, where endocardial and epicardial contours have been defined by an experienced cardiologist in all slices at the end of diastole and systole phases. All the images were obtained during 10–15 s breath-holds with a temporal resolution of 20 cardiac phases over the heart cycle. Cine steady state free precession (SSFP) MR short axis (SAX) images were obtained with a 1.5 T GE Signa MRI. For further details, please refer to Radau et al. [42]. In our experiment, datasets has been randomly divided into 4 groups for training and testing missions, 45 images in one group in which 15 for training and 30 for testing. All the pre-defined contours were confirmed by our cardiologists, which were utilized as the ground truth for evaluation purposes. The parameter φ_1 maintains 1 for all testing cases.

In addition to visual evaluation of accuracy, two quantitative measures were employed to compare the results achieved by our method with the ground truth: average perpendicular distance (APD) [39], and dice metric (DM) [24]. APD measures the perpendicular distances from points on result to the expert contour, and calculate the average value of them, with higher values implying that result doesn't match closely to the ground truth. DM measures the overlap rate of the areas surrounded by estimation and the truth. It ranges between 0 and 1, with higher DM indicating better match.

4.1. Initial epicardium estimation

In order to test accuracy of initial epicardium estimation, we intentionally selected some specific test instances, such as left ventricular abnormal hypertrophy shown in Fig. 3(c), whose endocardial contours are clearly different from the average in the given training group. In these cases, it is difficult to gain the accurate expression by sparse composition of the training repository. In fact, these situations can be regarded as large and not much sparse errors. In this stage, the epiccardium estimation is mainly depend on the endocardium, the spatial relationship between multiple shapes in SGC is not be fully used. However, the estimated result is still roughly confined in the myocardium region without leaking to surrounding tissues of LV. In order to achieve accurate delineation, we will refine them at the following iteration of segmentation by using the multiple shapes sparse modelling simultaneously. Three typical estimated epicardial contours are shown in Fig. 3(a–c) in contrast with expert contours, where Fig. 3(a) is good estimation with acceptable errors for estimation, while Fig. 3(c) shows a challenging case of the estimated results which achieves quite fallacious estimation. Fig. 3(b) and (c) need to be refined in the next stage. Estimation errors of 30 testing cases are shown in Fig. 4, where most APDs are lower than 3 mm (21 cases), DMs are higher than 0.92 (20 cases). Only 4 cases each of APDs are larger than 4 mm and DMs are smaller than 0.90. Mean values of APDs and DMs are 2.74 mm and 0.927, respectively.

4.2. Refinement results

We test different w_{endo} values to refine the intermediate deformation result after several iterations as a regularization step. Refined results of three typical estimated epicardial contours are shown in corresponding bottom row in Fig. 3 respectively, where Fig. 3(f) demonstrates the refined result of the challenging instance. Refined contour may not exactly match the image border due to the significant weak boundary, but achieved a reasonable accuracy. The other two cases (Fig. 3(d) and (e)) resulted in the better improved

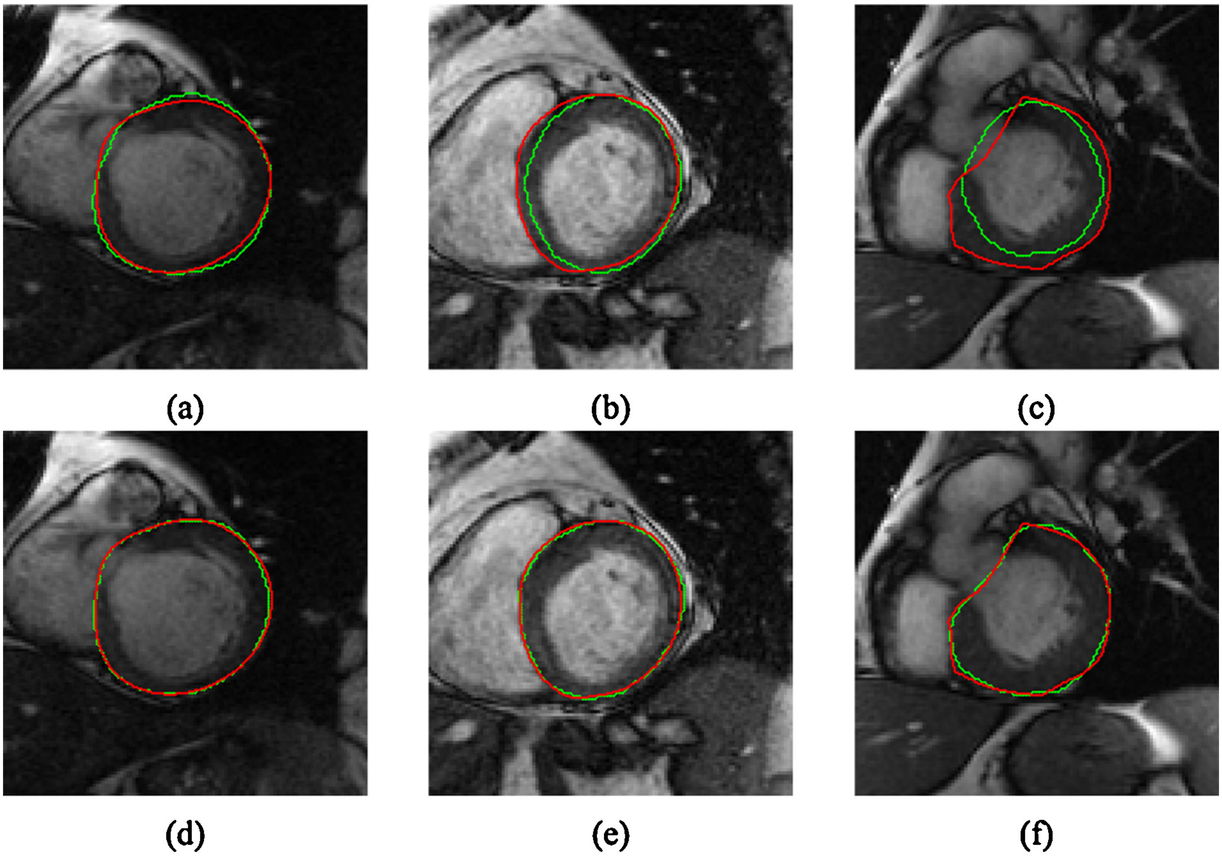

Fig. 3. Cases of estimation and corresponding refinement results. The top row shows estimated results and the bottom row shows relative refined results, respectively in green lines corresponding to expert contours in red lines. (a) Estimated contour closes to expert contour; (b) estimated contour roughly closes to expert contour; (c) challenged estimated contour; (d) refined result with respect to (a); (e) refined result with respect to (b); (f) refined result with respect to (c). (For interpretation of the references to color in this figure legend, the reader is referred to the web version of this article.)

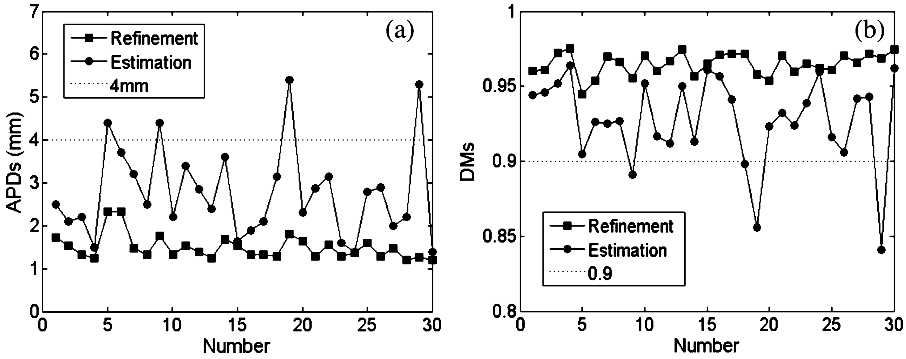

Fig. 4. Estimation and corresponding refinement errors of 30 testing cases. (a) average perpendicular distances; (b) dice metrics.

Table 2
Refinement for different w_{endo} values.

	$w_{endo}=0$	$w_{endo}=0.25$	$w_{endo}=0.5$	$w_{endo}=0.75$	$w_{endo}=1$
APD (mm)	2.05 ± 0.6	1.99 ± 0.6	1.94 ± 0.6	1.98 ± 0.6	1.95 ± 0.6
Average DM	0.947	0.950	0.952	0.949	0.951

Table 3
Refinement for different w_{endo} values with initial epicardial contour delineated manually.

	$w_{endo}=0$	$w_{endo}=0.25$	$w_{endo}=0.5$	$w_{endo}=0.75$	$w_{endo}=1$
APD (mm)	4.61 ± 2.52	3.45 ± 1.55	2.72 ± 0.91	2.50 ± 0.85	2.51 ± 0.87
Average DM	0.898	0.919	0.933	0.936	0.936

results. The statistical results are shown in Table 2. Compared with the conventional SSC, SGC achieves improved accuracies when regularizing the constraint deformation. The reason lies in the fact that only sparse and large errors can be eliminated by SSC when SGC can also catch not much sparse errors because the multiple shapes are represented simultaneously by sparse group composition of datasets. Refinement errors of 30 testing cases based on SGC with $w_{endo}=0.75$ are shown in Fig. 4, which reveals improved results compared to the initial estimation results.

In order to test the robustness of refinement based on the SGC, we randomly initialize a contour around LV manually instead of the initial estimated epicardium contour by the SGC. As demonstrated in Fig. 5, with valid representation and epi- and endocardium alignment, our approach can achieve a good match while the standard SSC fails. Actually, in more than half of all the 30 cases, where the deformation contains serious errors, the SSC can't regularize it into a reasonable result. With w_{endo} increases, which means endocardium and the spatial relationship between epi- and endocardium exert greater influence in the object function, refinement result generally becomes more close to the target. The ability makes SGC can significantly increase the segmentation robustness and the non-sensitivity to parameter setting in conjunction with shape-constraint CV or other segmentation methods. Statistical results are shown in Table 3, which reveals that, with the utilization of endocardium information and the a-prior spatial constraint, refinement based on SGC are more robust.

4.3. Segmentation result

Based on the framework in Section 3.2, epicardium of the basal slice is delineated. The examples with fuzzy border (a–o) and missing border (p–t) were chosen and their final segmentation results were demonstrated in Fig. 6, where the proposed SGC model and improved GCV model performed encouraging and the delineated epicardium boundaries corresponded well to the expert contours. The extracted contours were smooth and connected. The proposed method for effectively incorporating prior knowledge between LV epi- and endo-cardium helped delineation of epicardium in the vicinity of the lung where the image boundary is weak. And there are also good segmentation results when there are similar intensity between LV and right ventricle.

4.4. Comparative performance of segmentation accuracy

Experimental result of our method was compared with 9 recent methods from 2009 to 2014. Table 4 summarized the segmentation accuracy of above methods in terms of mean and standard deviation of the mean error and dice metric. Among these methods, most of them experimented on the datasets as same as ours, only [19,28,34] applied different datasets. All the methods, which we were employed in comparison, including image-based methods [9,15], graph-based methods [18,19,28], and model-based methods [34,44–46], can achieve acceptable segmentation accuracy. Compared to these state-of-the-art methods, our proposed method appeals competitive segmentation performance, which

Table 4
Comparative performance of segmentation accuracy.

Methods	Year	Mean error(mm)	DM
Wijnhout et al. [44]	2009	2.28 ± 0.39[a]	0.93 ± 0.01
Schaerer et al. [45]	2010	3.14 ± 0.33[a]	0.92 ± 0.02
Zhang et al. [34]	2010	1.81 ± 0.40[c]	0.92 ± 0.02
Huang et al. [15]	2011	2.22 ± 0.43[a]	0.93 ± 0.02
Mahapatra et al. [28]	2011	0.7 ± 0.3[b]	0.95 ± 0.01
Uzunbas et al. [18]	2012	1.78 ± 0.35[a]	0.91 ± 0.03
Hu et al. [9]	2013	2.21 ± 0.45[a]	0.94 ± 0.02
Abouzar et al. [19]	2013	1.48 ± 0.44[b]	~0.80
Sandro et al. [46]	2014	1.80 ± 0.41[a]	0.94 ± 0.02
Our method	**2015**	**1.50 ± 0.29**[a]	**0.96 ± 0.01**

[a] Average perpendicular distance (APD).
[b] Mean absolute distance (MAD).
[c] Average surface positioning error.

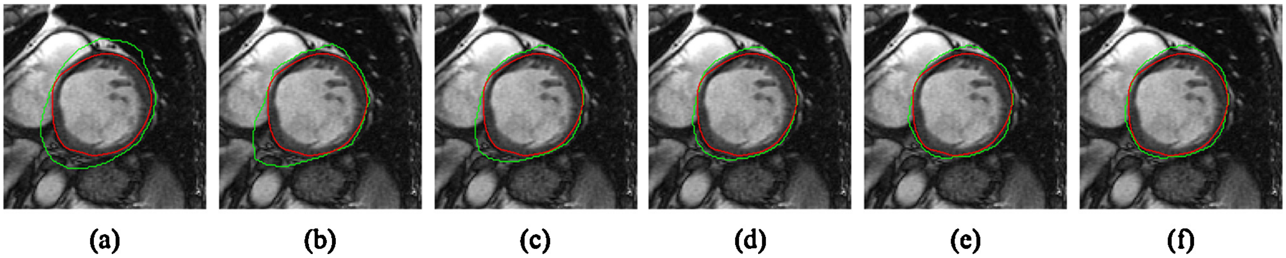

Fig. 5. Refinement on manual contour. Green line represents refinement result, while red line represents corresponding expert contour (a) manual contour; (b)refinement with $w_{\text{endo}} = 0$ (conventional SSC), APD = 7.30 mm; (c) $w_{\text{endo}} = 0.25$, APD = 4.43 mm;(d) $w_{\text{endo}} = 0.25$, APD = 3.19 mm;(e) $w_{\text{endo}} = 0.75$, APD = 2.88 mm;(f) $w_{\text{endo}} = 1$, APD = 2.77 mm. (For interpretation of the references to color in this figure legend, the reader is referred to the web version of this article.)

APD is 1.50 ± 0.29 mm, while DM is 0.96 ± 0.01. We owe such a good performance to the segmentation framework based on SGC, which remains the favourable algorithmic and numerical properties of SSC and further introduced additional advantages: without complicated manual landmark detection, and refinement reliability to even poor initial segmentation. The mean error and standard deviation in Table 4 shows that the proposed method achieved high level accuracy and robustness among all compared methods.

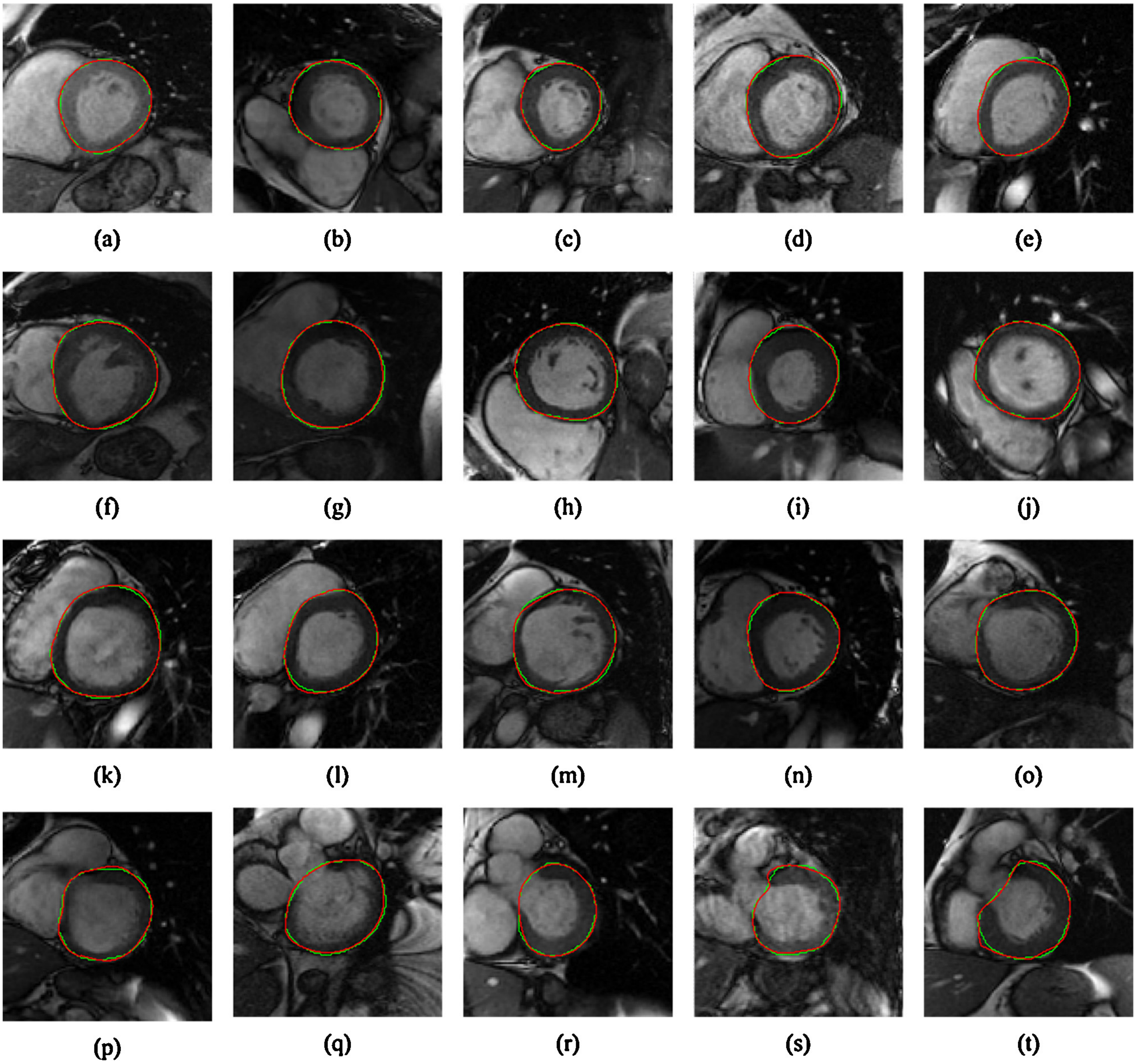

Fig. 6. Demonstration of final segmentation using our method. Green line represents segmentation result, while red line represents corresponding expert contour. (a)–(o) examples with fuzzy border; (p)–(t) examples with missing border. (For interpretation of the references to color in this figure legend, the reader is referred to the web version of this article.)

5. Conclusions

In this paper, we presented an extension method of SSC named as SGC model to simultaneously modeling multiple shapes priors. A framework of iterative procedure of SGC based refinement and GCV based deformation model is utilized for LV epicardium segmentation from cardiac MRI, in which epic- and endo-cardium act as a group to model together and an improved shape-constraint GCV acted as the deformation model. Experimental results demonstrate the good performance and strong robustness of our method which appeals promising potential for use in clinical practice.

In the future, we would like to improve our method in several aspects. Regarding to specific segmentation targets, we want to set up more suitable combination among multiple shapes to promote adaptability of the proposed method. Meanwhile, we want to apply this multi-shape model to more applications such as shape matching and registration. The SGC model also has a potential to be extended to 3D and 3D + Time applications.

Acknowledgements

This research is partially supported by the Chinese NSFC research fund (61375075, 61190120-61190124 and 61271318), the Natural Science Foundation of Hebei Province (F2012201020), and biomedical engineering fund of Shanghai Jiao Tong University (YG2012ZD06).

References

[1] World Health Organization. Global status report on noncommunicable diseases 2010. Geneva: World Health Organization; 2011.

[2] Mathers CD, Loncar D. Projections of global mortality and burden of disease from 2002 to 2030. PLoS Med 2006;3(11):e442.

[3] Petitjean C, Dacher J. A review of segmentation methods in short axis cardiac MR images. Med Image Anal 2011;15(2):169–84.

[4] Azhari HAIM, et al. Three-dimensional mapping of acute ischemic regions using MRI: wall thickening versus motion analysis. Am J Physiol 1990;259(5 Pt 2):H1492–503.

[5] Katouzian A, Prakash A, Konofagou E. A new automated technique for left and right-ventricular segmentation in magnetic resonance imaging. In: 28th annual international conference of the IEEE engineering in medicine and biology society. IEEE-EMBC; 2006. p. 3074–7.

[6] Pednekar A, Kurkure U, Muthupillai R, et al. Automated left ventricular segmentation in cardiac MRI. IEEE Trans Biomed Eng 2006;53(7):1425–8.

[7] Uzümcü M, van der Geest RJ, Swingen C, et al. Time continuous tracking and segmentation of cardiovascular magnetic resonance images using multidimensional dynamic programming. Invest Radiol 2006;41(1):52–62.

[8] Liu H, Hu H, Xu X, et al. Automatic left ventricle segmentation in cardiac MRI using topological stable-state thresholding and region restricted dynamic programming. Acad Radiol 2012;19(6):723–31.

[9] Hu H, Liu H, Gao Z, et al. Hybrid segmentation of left ventricle in cardiac MRI using gaussian-mixture model and region restricted dynamic programming. Magn Reson Imaging 2013;31:575–84.

[10] Rezaee M, van der Zwet P, Lelieveldt B, et al. A multiresolution image segmentation technique based on pyramidal segmentation and fuzzy clustering. IEEE Trans Image Process 2000;9(7):1238–48.

[11] Lynch M, Ghita O, Whelan P. Automatic segmentation of the left ventricle cavity and myocardium in MRI data. Comput Biol Med 2006;36:389–407.

[12] Cocosco C, Niessen W, Netsch T, et al. Automatic image-driven segmentation of the ventricles in cardiac cine MRI. J Magn Reson Imaging 2008;28(2):366–74.

[13] Fu J, Chai J, Wong S. Wavelet-based enhancement for detection of left ventricular myocardial boundaries in magnetic resonance images. Magn Reson Imaging 2000;18(9):1135–41.

[14] Jolly M, Xue H, Grady L, et al. Combining registration and minimum surfaces for the segmentation of the left ventricle in cardiac cine MR images. Med Image Comput Comput-Assist Intervention—MICCAI 2009;5762:910–8.

[15] Huang S, Liu J, Lee L, et al. An image-based comprehensive approach for automatic segmentation of left ventricle from cardiac short axis cine MR images. J Digit Imaging 2011;24(4):598–608.

[16] Boykov Y, Jolly M-P. Interactive organ segmentation using graph cuts. Med Image Comput Comput-Assist Intervention—MICCAI 2000;1935:276–86.

[17] Lin X, Cowan B, Young A. Model-based graph cut method for segmentation of the left ventricle. In: 27th annual international conference proceedings of the engineering in medicine and biology society. IEEE-EMBS; 2005. p. 3059–62.

[18] Uzunbas M, Zhang S, Pohl K, et al. Segmentation of myocardium using deformable regions and graph cuts. In: IEEE international symposium on biomedical imaging (ISBI). 2012. p. 254–7.

[19] Abouzar E, Athanasios K, Amin K, et al. Segmentation by retrieval with guided random walks: application to left ventricle segmentation in MRI. Med Image Anal 2013;17:236–53.

[20] Zhukov L, Bao Z, Guskov I, et al. Dynamic deformable models for 3D MRI heart segmentation. Proc SPIE 2002;4684:1398–405.

[21] Billet F, Sermesant M, Delingette H, et al. Cardiac motion recovery and boundary conditions estimation by coupling an electromechanical model and cine-MRI data. Proc Funct Imaging Model Heart 2009;5528:376–85.

[22] Gotardo P, Boyer K, Saltz J, et al. A new deformable model for boundary tracking in cardiac MRI and its application to the detection of intraventriculardyssynchrony. Comput Vision Pattern Recognit—CVPR 2006;1:736–43.

[23] El Berbari R, Bloch I, Redheuil A, et al. An automated myocardial segmentation in cardiac MRI. In: 29th annual international conference of the IEEE engineering in medicine and biology society. IEEE-EMBS; 2007. p. 4508–11.

[24] Lynch M, Ghita O, Whelan P. Segmentation of the left ventricle of the heart in 3-D + t MRI data using an optimized nonrigid temporal model. IEEE Trans Med Imaging 2008;27(2):195–203.

[25] Leventon ME, Grimson WEL, Faugeras O. Statistical shape influence in geodesic active contours. In computer vision and pattern recognition, 2000. ProcIEEE Conf IEEE 2000;1:316–23.

[26] Cremers D, Tischhäuser F, Weickert J, Schnörr C. Diffusion snakes: introducing statistical shape knowledge into the Mumford-Shah functional. Int J Comput Vision 2002;50(3):295–313.

[27] Mumford D, Shah J. Optimal approximations by piecewise smooth functions and associated variational problems. Commun Pure Appl Math 1989;42(5):577–685.

[28] Mahapatra D, Sun Y, Orientation. Histograms as shape priors for left ventricle segmentation using graph cuts. Med Image Comput Comput-Assist Intervention—MICCAI 2011;6893:420–7.

[29] Wu Y, Wang Y, Jia Y. Segmentation of the left ventricle in cardiac cine MRI using a shape-constrained snake model. Comput Vision Image Understanding 2013;117(9):990–1003.

[30] Cootes T, Taylor C. Active shape models-smart snakes. In: British machine vision conference—BMVC. 1992.

[31] Cootes T, Edwards G, Taylor C. Active appearance models. In: European conference on computer vision—ECCV. 1998. p. 484–98.

[32] Mitchell S, Lelieveldt B, van der Geest R, et al. Multistage hybrid active appearance model matching: segmentation of left and right ventricles in cardiac MR images. IEEE Trans Med Imaging 2001;20(5):415–23.

[33] Mitchell S, Bosch J, Lelieveldt B, et al. 3-D active appearance models: segmentation of cardiac MR and ultrasound images. IEEE Trans Med Imaging 2002;21(9):1167–78.

[34] Zhang H, Wahle A, Johnson RK, et al. 4-D cardiac MR image analysis: left and right ventricular morphology and function. IEEE Trans Med Imaging 2010;29(2):350–64.

[35] Lorenzo-Valdes M, Sanchez-Ortiz G, Elkington A, et al. Segmentation of 4D cardiac MR images using a probabilistic atlas and the EM algorithm. Med Image Anal 2004;8(3):255–65.

[36] Zhang S, Uzunbas M, Yan Z, et al. Construction of left ventricle 3D shape atlas from cardiac MRI. Functional Imaging and Modeling of the Heart, vol. 6666. Springer Berlin Heidelberg; 2011. p. 88–94.

[37] Zhang S, Zhan Y, Dewan M, Huang J, Metaxas DN, Zhou XS. Towards robust and effective shape modeling: sparse shape composition. Med Image Anal 2012;16(1):265–77.

[38] Zhang S, Zhan Y, Metaxas DN. Deformable segmentation via sparse representation and dictionary learning. Med Image Anal 2012;16(7):1385–96.

[39] Goodall C. Procrustes methods in the statistical analysis of shape. J R Stat Soc, Ser B: Methodol 1991;53(2):285–339.

[40] Guo Yiting, et al. Semiautomatic segmentation of aortic valve from sequenced ultrasound image using a novel shape-constraint GCV model. Med Phys 2014;41.7:072901.

[41] Chan T, Vese L. Active contours without edges. IEEE Trans Image Process 2001;10(2):266–77.

[42] Radau P, Lu Y, Connelly K, et al. Evaluation Framework for Algorithms Segmenting Short Axis Cardiac MRI. The MIDAS Journal—Cardiac MR Left Ventricle Segmentation Challenge; 2009. http://hdl.handle.net/10380/3070

[43] HeimannT MeinzerH. Statistical shape models for 3D medical image segmentation: a review. Med Image Anal 2009;13(4):543–63.

[44] Wijnhout J, Hendriksen D, Assen H, et al. LV challenge LKEB contribution: fully automated myocardial contour detection. Midas J 2009;43:683.

[45] Schaerer J, Casta C, Pousin J, et al. A dynamic elastic model for segmentation and tracking of the heart in MR image sequences. Med Image Anal 2010;14:738–49.

[46] Sandro Q, Daniel B, Brecht H, et al. Fast automatic myocardial segmentation in 4D cine CMR datasets. Med Image Anal 2014;18:1115–31.

[47] Rousson M, Paragios N. Shape priors for level set representations. In: In Computer Vision—ECCV 2002. Springer Berlin Heidelberg; 2002. p. 78–92.